scientific reports

Check for updates

OPEN

Noise reduction method for mine wind speed sensor data based on CEEMDAN-wavelet threshold

Yu Wang[1,2], Jian Liu[1,2]✉, Dong Wang[1,3], Xue Liu[1,2], Peng Cao[1,2] & Kunpeng Hua[4,5]

The mine wind speed sensor is an important intelligent sensing equipment in the mine intelligent ventilation system that can provide accurate and key wind speed parameters for the intelligent ventilation system. The turbulent pulsation characteristics of the airflow in the underground tunnel are a major factor for the inaccurate measurement of mine wind speed. Therefore, according to the random non-stationary characteristics of a turbulent pulsation signal, a denoising method based on adaptive complete ensemble empirical mode decomposition (CEEMDAN) combined with the wavelet threshold is proposed for suppressing the turbulent pulsation noise in the wind speed signal. First, the CEEMDAN algorithm is used for decomposing the wind speed signal into a series of IMF components. Second, the continuous mean square error criterion is used for determining the high-frequency IMF components with more noise. The wavelet threshold denoising method is used for denoising the high-frequency IMF components with more noise. Finally, the denoised IMF components and remaining low-frequency IMF components are reconstructed for obtaining the denoised signal. The results of the denoising analysis of measured turbulent pulsation signals, comparative analysis of denoising of simulated turbulent pulsation signals by different joint denoising methods, and denoising analysis of actual mine wind speed sensor data indicate that the joint denoising method proposed in this study has a higher signal-to-noise ratio and lower root mean square error of the wind speed signal after denoising. Compared with the EMD-wavelet threshold and EEMD-wavelet threshold denoising methods, the denoising method proposed in this study is better and has higher denoising accuracy, which provides a new method for processing actual mine wind speed sensor data.

Keywords Mine intelligent ventilation, Mine wind speed sensor, CEEMDAN, Wavelet threshold, Data noise reduction

Coal mine intelligence is a core technical support for the high-quality development of the coal industry[1]. Intelligent ventilation systems are important subsystems in intelligent mines. However, the size and changes of tunnel wind speed and air volume are the basic parameters for the calculation of mine ventilation networks, an important indicator for evaluating the stability of mine ventilation systems, and an important basic data for self-learning of intelligent ventilation systems, which directly affects whether mine safety production can proceed smoothly. As a key intelligent sensing equipment in the intelligent ventilation system, the mine wind speed sensor monitors the wind speed and its changes in the main tunnels underground in real time and uploads them to the ground control center, providing key wind speed data for the intelligent program of the computer in the control center. It is responsible for mapping the real status of the underground ventilation system in real time. However, the complex and changeable underground environment introduces considerable noise and disturbance to the wind speed sensor, seriously affecting intelligent ventilation during normal production and emergency wind control during disasters. Therefore, in the construction of intelligent ventilation systems in mines, the wind speed sensor must have a noise reduction function and report more accurate test data after noise reduction to the centralized control center for providing key, accurate, and effective monitoring data for on-demand air supply, real-time network solutions, intelligent identification of wind flow disturbances, intelligent reconstruction of ventilation systems, and intelligent decision-making and control of mines[2,3].

[1]College of Safety Science and Engineering, Liaoning Technical University, Huludao 125105, Liaoning, China. [2]Key Laboratory of Mine Thermo-Motive Disaster and Prevention, Ministry of Education, Huludao 125105, Liaoning, China. [3]Liaoning Academy of Mineral Resources Development and Utilization Technical and Equipment Research Institute, Liaoning Technical University, Fuxin 123000, China. [4]CCTEG Changzhou Research Institute, Changzhou 213015, Jiangsu, China. [5]Tiandi (Changzhou) Automation Co, Ltd, Changzhou 213015, Jiangsu, China. ✉email: liujian@lntu.edu.cn

During the normal production period of a mine, the passage of personnel and mine cars, opening and closing of dampers, lifting of cages, and resistance-type faults in tunnels[4,5] cause the wind speed sensor monitoring data for undergoing waveform changes with their own characteristics. These disturbances are key data to achieve on-demand air supply, real-time ventilation network solutions, intelligent reconstruction of the ventilation system, intelligent identification of wind flow disturbances, and disaster warning. However, in the process of denoising the monitoring data from mine wind-speed sensors, these fluctuations may be regarded as noise and eliminated if the denoising method or algorithm parameters are not properly selected. Therefore, scholars conducted extensive research on the denoising and disturbance identification of mine wind-speed sensor monitoring data. Huang et al.[6] automatically adjusted the process noise covariance and measurement noise covariance based on the difference between the measured and expected speed signals and established an adaptive Kalman filter. This filter can effectively eliminate abnormal data from wind speed sensors, reduce the root mean square error (RMSE), improve the accuracy of instantaneous wind speed monitoring, and predict short-term wind speeds. Li et al.[7], based on an improved Kalman filter can identify dynamic errors in ventilation systems, proposed a real-time correction method that uses wind speed sensors for accurately and comprehensively collecting mine air volume data. Based on the node air volume balance principle, they proposed the network solution correction method that involves three sensor redundant arrangements, significantly improving both the sensor testing accuracy and network solution accuracy. Zhao et al.[8] proposed a wind-speed sensor monitoring data-cleaning model based on a stacked denoising autoencoder (SDAE). The SDAE algorithm was used to train sample data under normal ventilation conditions, and the kernel density estimation was used to obtain the upper limit of the reconstruction error. Subsequently, an apriori algorithm was used to monitor the correlation between the data time series. The model can automatically identify outliers and missing values, providing reliable data for ventilation system fault diagnosis and disaster warning. Li et al.[9] proposed a singular spectrum analysis (SSA)-long short-term memory (LSTM) wind speed abnormal fluctuation detection method based on the combination of SSA and an LSTM neural network. A comparative analysis revealed that the proposed method has a better reconstruction effect than the ARIMA, BP, and CNN models, with an anomaly detection accuracy of 99.2% and an F1-Score of 0.97. Wei et al.[10,11] used three smoothing and denoising methods, FCM, Rloess, and S-G for analyzing and processing the measured wind speed data, and they concluded that FCM is superior when processing abnormal wind speed data caused by process variables. Further, it is reasonable to use the loess algorithm or the S-G algorithm when processing abnormal wind speed data caused by state variables. The FCM-Rloess or FCM-SG algorithms can be used in combination when processing abnormal wind speed data caused by both process and state variables.

In mine ventilation systems, the wind flow at most underground locations is in a completely turbulent state; i.e., except in front of the damper or in the chamber where the wind speed is extremely low and the wind flow in the mine tunnels is turbulent. The pulsating characteristics of turbulence caused the mine wind speed sensor for fluctuating continuously around the current average wind speed. However, the constantly changing indication of wind speed caused by turbulence pulsation is not the data required by engineering practice. Therefore, this paper regards turbulence pulsation as a kind of "noise" to reduce the noise of wind speed signal and minimize the impact of turbulence pulsation on wind speed sensor as much as possible. Liu et al.[12] used a laser Doppler anemometry (LDA) system to test the pulsation phenomenon of the turbulent state of wind flow in a straight mine tunnel without external disturbance. The test results indicate that when the average wind speed is 2.57 m/s, the maximum pulsation amplitude of the wind speed is as high as 1.19 m/s even if the effect of production activities such as the passage of personnel and mine cars, damper switches, and cage lifting is eliminated. Consequently, an underground wind speed sensor cannot provide accurate wind speed and air volume parameters for intelligent ventilation links, such as high-performance real-time ventilation network solutions[13]. Further, it cannot effectively map the status of the underground ventilation system. Simultaneously, the test experiment revealed that the amplitude of the turbulent pulsation signal obeyed a normal distribution, and the power spectrum density was uniformly distributed, as shown in Fig. 1. This vibration with a normal amplitude and uniform power spectrum density in the signal field is Gaussian white noise, which provides a theoretical basis for selecting noise reduction methods for downhole wind speed sensor data.

Compared with the traditional Fourier transform, the wavelet transform is a local transform in the time and frequency domains, and it can therefore effectively extract information from signals. Further, the wavelet

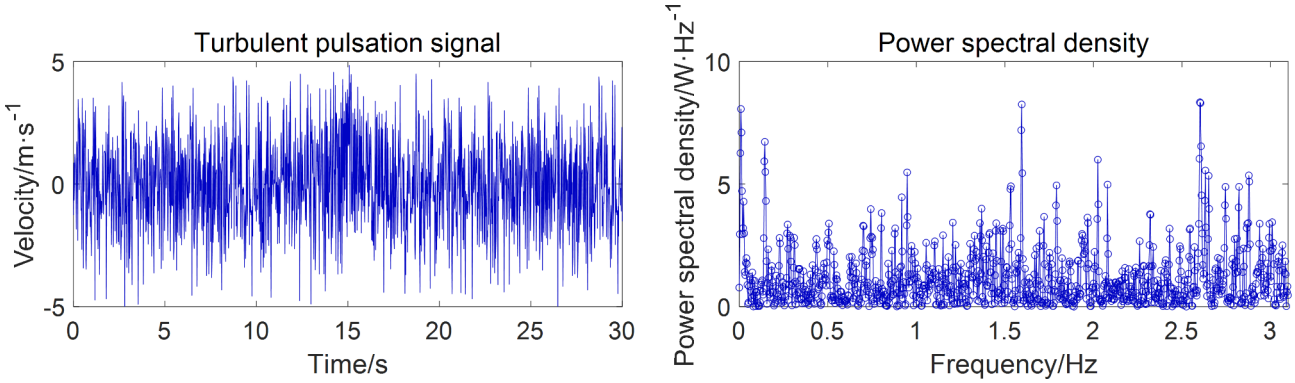


Fig. 1. Turbulent pulsation signal waveform and power spectral density.

transform can perform a multiscale refinement analysis of functions or signals through operations such as scaling and translation. In the field of signal analysis, it is widely used in boundary processing and filtering, time-frequency analysis, signal-to-noise separation and extraction of weak signals, calculation of the fractal index, signal recognition and diagnosis, and multi-scale edge detection. Ying et al.[14] proposed a DSP-based wavelet transform instruction cycle model as a basis for real-time evaluation, compared the real-time performance of different wavelet al.gorithms, and proposed a comprehensive evaluation index based on the coefficient of variation weighting method according to the characteristics of the collected diesel engine cylinder head vibration signal. The wavelet basis function was optimized from the perspectives of noise reduction and real-time performance. Liu et al.[15] proposed a wavelet denoising algorithm with parameter optimization and experimentally verified that the algorithm has a good filtering effect and certain application value in extracting the height of ground objects by waveform decomposition. Priyadarshini et al.[16] used Fourier, short-time Fourier, continuous and discrete wavelet transforms for transforming and processing power quality disturbances, respectively. Energy values and 3D graphs obtained by each method were compared, analyzed, and explained, which helped fully understand the power-quality disturbances. Baorui et al.[17] proposed an acceleration-guided acoustic signal denoising framework (AG-ASDF) based on a learnable wavelet transform and evaluated the effectiveness of slab track condition detection based on acoustic signals using a multiclass support vector machine (SVM). Compared with other feature extraction and learning methods, the accuracy of this method was significantly improved. Dodda et al.[18] proposed an attention-based wavelet convolutional neural network (AWUN) method for the simultaneous denoising and reconstruction of incomplete seismic data. Quantitative results indicate that this method exhibits a higher signal-to-noise ratio (SNR) and mean square error (MSE) compared with the existing state-of-the-art methods. It can be seen that wavelet transform is widely used and studied in the analysis and processing of non-stationary signals[19–22], and the wavelet threshold has a good effect on the noise reduction of white Gaussian noise. Therefore, adopting the wavelet threshold noise reduction method to reduce the noise of turbulent pulsation noise similar to white Gaussian noise can effectively improve the quality and accuracy of wind speed signal of wind speed sensor. However, the selection of relevant parameters when using the wavelet transform to analyze and process signals has low generalization. For example, in the process of signal denoising using the wavelet threshold method, the improper selection of the basis function, decomposition level, threshold criterion, and threshold function has a significant impact on the denoising effect. Therefore, the relevant parameters should first be optimized or improved when using the wavelet transform for signal analysis and processing. Further, it can be analyzed and processed in combination with other advantageous decomposition methods based on the signal characteristics[23–25].

Since Huang et al.[26] proposed the empirical mode decomposition (EMD) algorithm in 1998, the EMD series of decomposition algorithms has been applied by many scholars to signal denoising, filtering, and recognition in various fields[27–35]. The EMD algorithm decomposes signals based on the time-scale characteristics of the data without presetting the basis functions. This is different from Fourier and wavelet decompositions based on a priori harmonic and wavelet basis functions. Therefore, the EMD method can be theoretically applied to the decomposition of any type of signal, and it has obvious advantages in processing nonstationary and nonlinear data. However, there is an inevitable flaw in the EMD method[36]. The original signal must satisfy the decomposability condition when the trend term is extracted; otherwise, it can lead to modal aliasing. To avoid this phenomenon, an ensemble empirical mode decomposition (EEMD) algorithm was proposed to improve EMD in 2009[37]. The main improvement of EEMD is to use the characteristic that the mean of the white noise is zero and artificially introduce uniformly distributed white noise multiple times during the decomposition process for covering up the noise of the signal itself and obtain more accurate upper and lower envelopes. The decomposition results were averaged simultaneously. The higher the average processing time, the smaller is the impact of noise on the decomposition. However, a greater number of average processing times will result in a greater amount of computation to minimize the impact of noise on the decomposition. Subsequently, the team proposed an improved EEMD algorithm, CEEMD[38], in 2010. The idea of the improvement is similar to that of EEMD; however, it introduces positive and negative complementary white noise for reducing the computational complexity of the decomposition process. Although the EMD algorithm has been improved twice, there will always be a certain amount of white noise remaining in intrinsic mode components obtained by decomposing the signal, thereby affecting signal analysis and processing. Torres et al.[39] proposed a complete ensemble empirical mode decomposition with adaptive noise (CEEMDAN) based on EMD in 2011 to solve the problems of modal aliasing and residual white noise in the decomposition process. They borrowed the idea of adding Gaussian noise and multiple superposition and averaging for offsetting the noise in the EEMD method. The CEEMDAN decomposition algorithm adds noisy modal components after EMD at each iteration instead of directly adding Gaussian white noise to the original signal. The first-order modal components obtained from each decomposition are averaged to obtain the final first-order modal components. Then, this operation is repeated on the residual parts, effectively solving the problem of a certain amount of white noise remaining in each modal component and reducing the computational cost.

Extensive research has been conducted on signal analysis and processing in various fields from the aspects of theoretical algorithms, simulation and emulation, experiments, and field verification; however, no theoretical basis has been proposed to determine the nature of mine wind speed sensor signal noise. Aiming at the turbulent pulsation characteristics of airflows in mine tunnels, this study used the CEEMDAN decomposition algorithm combined with wavelet threshold denoising to study the denoising method for mine wind speed sensor monitoring data. Thus, the proposed method is a key intelligent sensing device for mine ventilation systems with intelligent data analysis and processing functions that can provide accurate and effective data for on-demand air supply, real-time network solutions, intelligent identification of wind flow disturbances, and intelligent reconstruction of ventilation systems. It is of great significance to realize the "unmanned monitoring

and perception, intelligent analysis and decision making, and automated remote control and joint control" of mine ventilation.

Method

CEEMDAN decomposition algorithm

Let imf_k represent the kth modal component obtained by the CEEMDAN decomposition method and $v'(t)$ represent the noise signal attached to the simulation signal $v(t)$. This paper uses LDA to test the wind speed pulsation signal in an undisturbed straight tunnel and Gaussian white noise automatically generated by the algorithm that satisfies the standard normal distribution. The CEEMDAN decomposition algorithm process is shown in Fig. 2. According to the denoising method, the specific implementation steps of the algorithm are as follows:

(1) Add I positively and negatively paired auxiliary white noise sequences $m^i(t)$ to the original signal to be processed $V(t) = v(t) + v'(t)$; construct a new signal $V(t) + (-1)^b a_0 m^i(t)$, $i = 1, 2, \cdots, I$; perform EMD decomposition on the signal; and after M iterations, obtain I first-order components $imf_1^i(t)$, as shown in

$$V(t) + (-1)^b a_0 m^i(t) = imf_1^i(t) + res_1^i(t), \tag{1}$$

where $m^i(t)$ represents the white noise sequence added in the i-th decomposition; a_0 represents the noise amplitude, which is controlled by the standard deviation of the noise signal and simulation signal; b is 1 or 2 to ensure that the noise is added in positive and negative pairs; and $res_1^i(t)$ represents the first remaining residual.

The final modal component $IMF_1(t)$ is obtained by taking the average of the I first-order component $imf_1^i(t)$ as

$$IMF_1(t) = \frac{1}{I}\sum_{i=1}^{I} imf_1^i(t) = V(t) - \frac{1}{I}\sum_{i=1}^{I} res_1^i(t). \tag{2}$$

Equations (1) and (2) indicate that positive and negative white noise can cancel each other out when calculating the mean, thereby significantly reducing the noise content of the $IMF_1(t)$.

(2) Combining Eqs. (1) and (2), the final first-stage residual can be calculated as

$$res_1(t) = V(t) - IMF_1(t) = \frac{1}{I}\sum_{i=1}^{I} res_1^i(t). \tag{3}$$

Adding the positively and negatively paired white noise *IMF* signals obtained by EMD decomposition to $res_1(t)$, the composition signal becomes $res_1(t) + (-1)^b a_1 E_1(m^i(t))$, and then, decomposing it again, the second-order component $imf_2^i(t)$ can be obtained as

$$res_1(t) + (-1)^b a_1 E_1(m^i(t)) = imf_2^i + res_2^i(t). \tag{4}$$

The final second-order component $IMF_2(t)$ was obtained by averaging $Iimf_2^i(t)$as

$$IMF_2(t) = \frac{1}{I}\sum_{i=1}^{I} imf_2^i(t) = res_1(t) - \frac{1}{I}\sum_{i=1}^{i} r_2^i(t). \tag{5}$$

The second-order residual can be obtained as

$$res_2(t) = res_1(t) - IMF_2(t) = \frac{1}{I}\sum_{i=1}^{I} r_2^i(t). \tag{6}$$

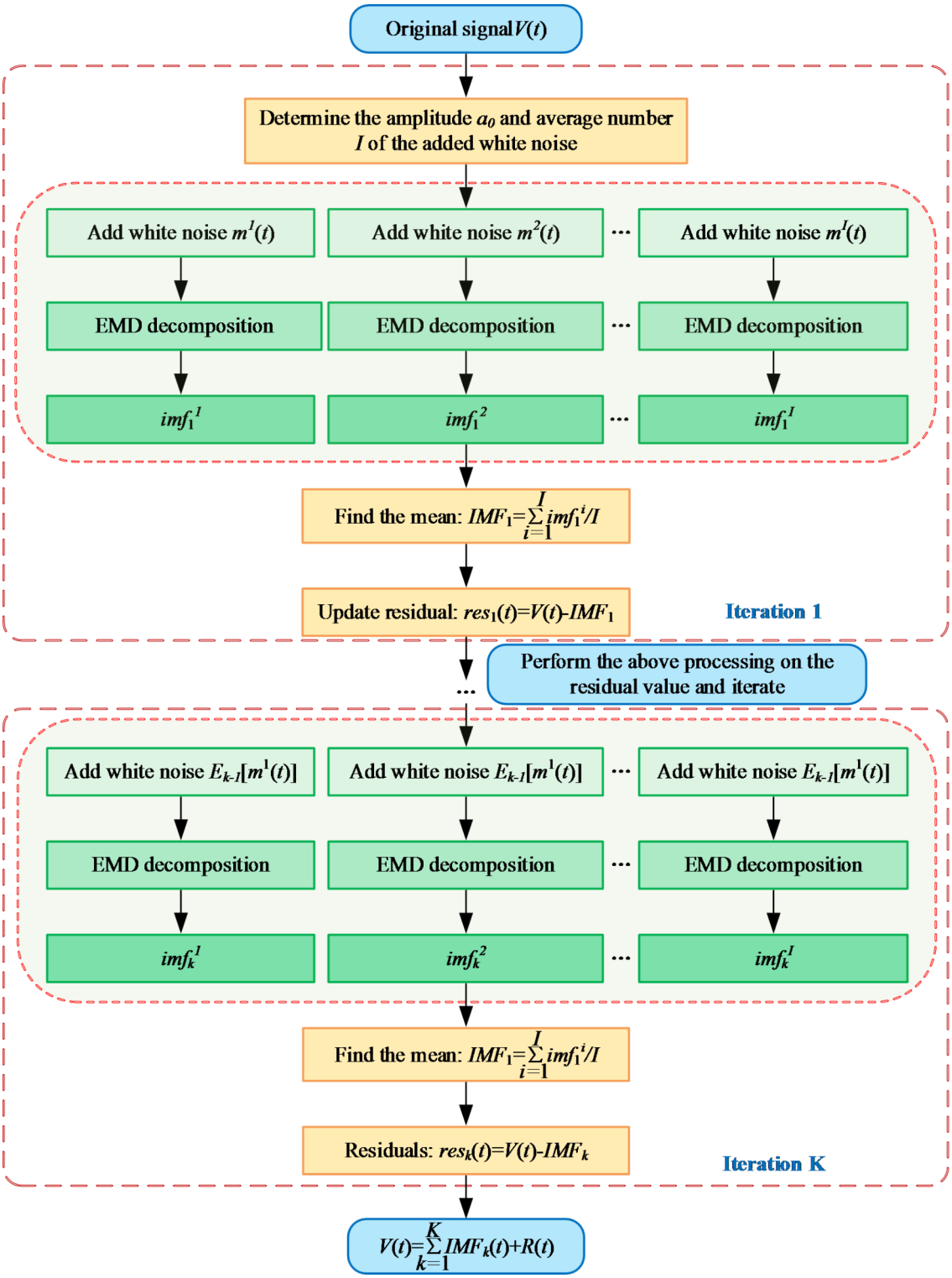


Fig. 2. CEEMDAN algorithm flowchart.

(3) Steps 1 and 2 are repeated. $kIMF$ components are obtained when the number of the extreme points of the residual component $res_k(t)$ is less than two. The final residual $R(t)$ obtained by the entire decomposition process, i.e., the initial signal, can be expressed as

$$V(t) = \sum_{k=1}^{K} IMF_k(t) + R(t). \tag{7}$$

Identification of critical IMF components

Determining the boundary between the high IMF component and low-frequency IMF components after the CEEMDAN decomposition, removing the IMF components with more noise above this boundary, and recombining the remaining IMFs to achieve noise removal is necessary for realizing the best noise reduction effect. This study refers to a method proposed by Boudraa to find the critical IMF component[40], and it uses formula (8) to solve the continuous mean square error (CMSE) of each IMF component, i.e., the dividing point k where the signal and noise play a dominant role is the global minimum position of the IMF energy.

$$CMSE(x_k, x_{k+1}) = \frac{\sum_{n=1}^{N} [x_k(n) - x_{k+1}(n)]^2}{N}, \tag{8}$$

where $x_k(n)$, $x_{k+1}(n)$, and n represent the amplitude of the n-th sampling point of the k-th IMF quantity, amplitude of the n-th sampling point of the $(k+1)$-th IMF quantity, and sampling length, respectively.

The dividing point between the high- and low-frequency IMF components after signal decomposition is

$$c = \arg_{1 \leqslant k \leqslant n-1} \min \left[CMSE\left(x_k, x_{k+1}\right) \right]. \tag{9}$$

The boundary point c, where the signal and noise play a leading role, is the global minimum position of the continuous mean square error of all IMF components. Therefore, from the first IMF component to the c IMF component, it is determined as the high frequency IMF component. This method solves the problem of poor noise reduction effect caused by artificially determining the critical point.

Wavelet threshold denoising

The high-frequency IMF components after the CEEMDAN decomposition can be obtained using a discrete wavelet transform as

$$w_f\left(j,k\right) = w_s\left(j,k\right) + w_n(j,k)'\left(j = 0,1,2,\ldots,J; k = 0,1,2,\ldots,N\right), \tag{10}$$

where J represents the maximum decomposition level of the wavelet transform; N represents the length of the signal; and $w_f\left(j,k\right)$, $w_s\left(j,k\right)$, and $w_n\left(j,k\right)$ represent the wavelet coefficients of the noisy signal, original signal, and noise at the j-th layer, denoted as $\omega_{j,k}$, $\mu_{j,k}$, and $\upsilon_{j,k}$, respectively.

The key to wavelet thresholding is selecting a suitable threshold T to perform threshold quantization processing on the wavelet coefficient $\omega_{j,k}$ of a noisy signal to make it as close as possible to the wavelet coefficient $.w_s\left(j,k\right)$. of the original signal. The processed threshold can be expressed as$\hat{\omega}_{j,k}$, and the wavelet reconstruction is performed for obtaining the denoised signal.

(1) Currently, there is no fixed theoretical standard for selecting a wavelet basis. In the field of signal denoising, a discrete orthogonal wavelet basis is often used considering that the continuous wavelet transform is redundant and increases the difficulty of signal analysis. The widely used discrete wavelet basis functions include the Daubechies, Symlets, Coiflets and Biorthogonal series wavelet families.
(2) The effect of the number of decomposition layers cannot be ignored when performing high-precision noise reduction on mine wind-speed data. The SNR of the signal after noise reduction is not effectively improved when the number of decomposition layers is too small, and the purpose of signal noise reduction cannot be achieved easily. However, the number of decomposition layers should not be too large because too many decomposition layers will cause a loss of effective information in the wind speed data. Therefore, the number of decomposition layers ranging from 1 to 10 can be compared with the noise reduction results for optimizing the number of decomposition layers.
(3) There are four widely used threshold selection methods for wavelet threshold denoising, which are listed below:

    a. Unbiased risk estimation threshold (Rigrsure).

    The Rigrsure threshold is defined as

$$T = \sigma\sqrt{\gamma(k_{\min})}(k = 1, 2, \ldots, N), \tag{11}$$

where σ and $\gamma(k)$ represent the variance of the noise and signal sequence obtained by taking the absolute value of each element in the signal, sorting them by size, and taking the square. For the threshold $T_k = \sigma\sqrt{\gamma(k)}$, the value corresponding to the minimum risk point according to the risk it generates is $k_{\min}$.

b. Fixed threshold (Sqtwolog).

This criterion uses a fixed threshold as

$$T = \sigma\sqrt{2\ln N}. \tag{12}$$

c. Heuristic threshold (Heursure).

The heuristic threshold is a combination of the first two thresholds, setting two variables $\eta = \sqrt{\frac{1}{N}(\log_2 N)^3}$, $\mu = \frac{1}{N}\left(\sum_{j=1}^{N}|s_j|^2 - N\right)$, and then, the heuristic threshold is defined as

$$T = \begin{cases} \sigma\sqrt{2\ln N}, & if \quad (\mu < \eta) \\ Min\left(\sigma\sqrt{2\ln N}, \sigma\sqrt{\gamma(k_{\min})}\right), & else \end{cases} \tag{13}$$

d. Minimaxi threshold (Minimaxi).

This criterion also uses a fixed threshold defined as

$$T = \begin{cases} \sigma(a + b\log_2 N), & if \quad (N > 32) \\ 0, & else \end{cases}, \tag{14}$$

where $a = 0.3036$ and $b = 0.1829$.

(4) Two commonly used threshold quantization functions are used for the threshold shrinkage processing of wavelet coefficients, as listed below.

a. Hard threshold

$$\hat{\omega}_{j,k} = \begin{cases} \omega_{j,k}, & if \quad (|\omega_{j,k}| > T) \\ 0, & else \end{cases} \tag{15}$$

where λ represents the threshold value.

b. Soft threshold

$$\hat{\omega}_{j,k} = \begin{cases} \operatorname{sgn}(\omega_{j,k})(|\omega_{j,k}| - \lambda), & if \quad (|\omega| \geqslant T) \\ 0, & else \end{cases} \tag{16}$$

CEEMDAN-wavelet threshold joint denoising

The process of denoising the wind-speed sensor data using the CEEMDAN-wavelet threshold joint denoising method is shown in Fig. 3. The steps are as follows:

(1) Perform CEEMDAN decomposition on the wind-speed sensor signal $V(t)$ to obtain intrinsic mode function components IMF_k from high to low frequencies.

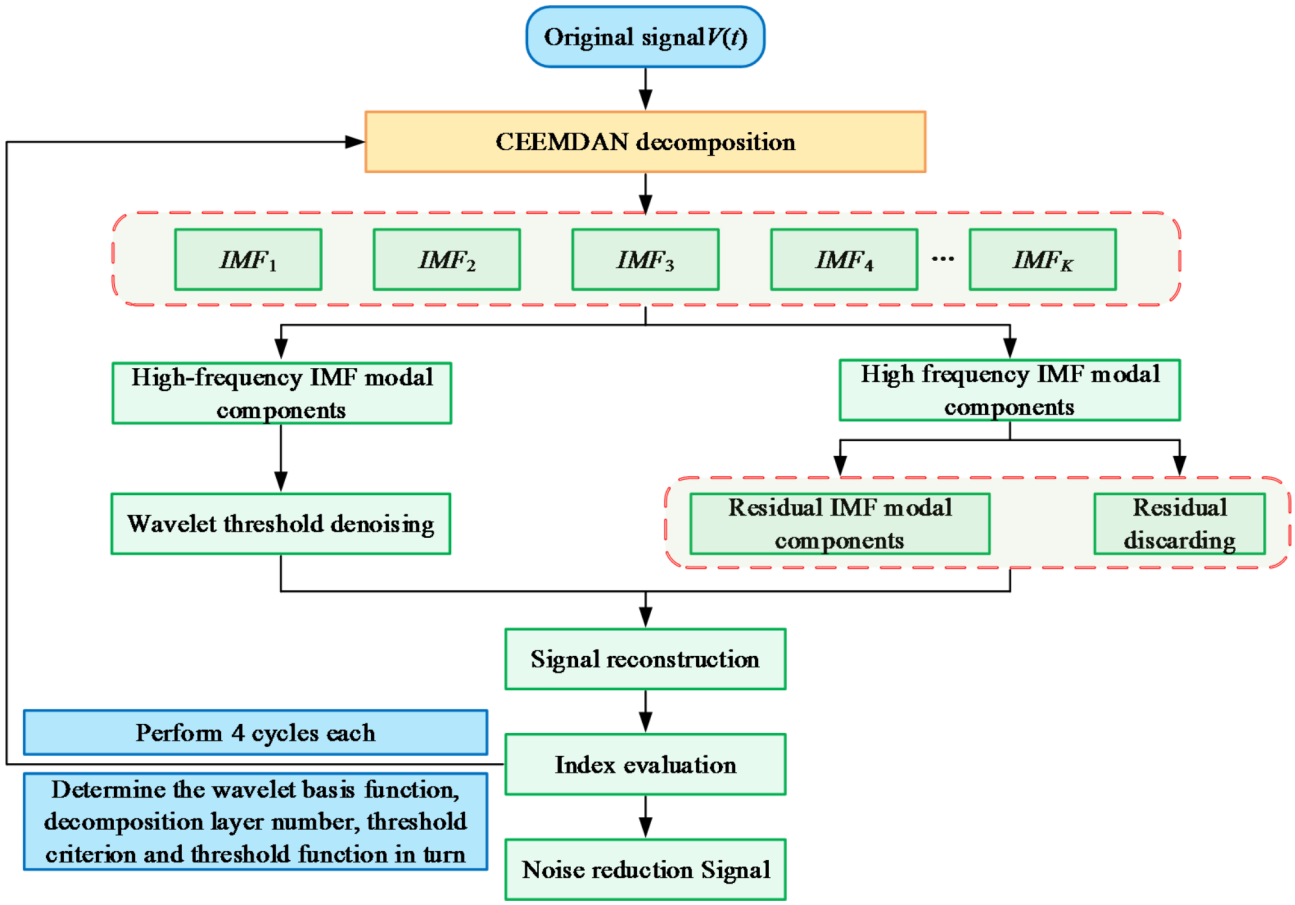


Fig. 3. CEEMDAN: Flowchart of wavelet threshold denoising method.

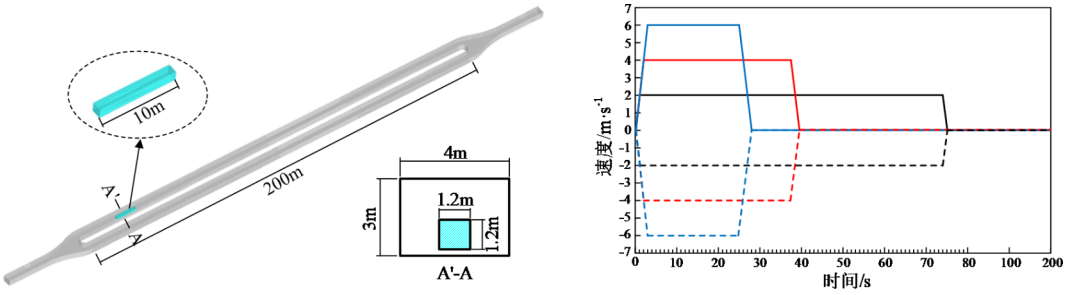


Fig. 4. Simulated tunnel physical model.

(2) High-frequency IMF_k components that need to be denoised by the wavelet threshold are screened using a CMSE.
(3) Different wavelet threshold parameters are used to denoise the screened high-frequency IMF_k components.
(4) The wavelet signal is reconstructed, and the high-frequency IMF_k component after noise reduction is obtained.
(5) The high-frequency IMF_k component and the remaining low-frequency IMF_k component after noise reduction by wavelet threshold are reconstructed, and the high-frequency IMF_k component after noise reduction is directly added with the remaining low-frequency IMF_k component, so as to obtain the denoised signal.
(6) Evaluate the signal indicators after noise reduction and repeat steps (1)–(6) using the optimal parameters in step (3) until the parameters in step (3) are optimal.

Data collection

The fluid simulation software Fluent was used to perform dynamic mesh simulation calculations for the passage of mine cars in parallel tunnels. The monitoring points were set at an average wind speed circle close to the

roof for monitoring the wind speed when the mine cars passed through the tunnel. The calculation model used the standard k-epsilon and selected the velocity-pressure coupled SIMPLE algorithm, second-order pressure interpolation method, and second-order upwind format. The residual convergence was set to 10^{-4} and the calculation was set to start from the entire domain (all zones) during initialization. The default initialization setting was used to calculate the turbulent kinetic energy and turbulent kinetic energy dissipation rate for the entire domain.

Considering that both the experimental and actual mine ventilation are subsonic flows, i.e., the gas in the calculation domain is not subject to volume compression and expansion, the gas is set to an incompressible ideal gas model, density is set to 1.225 kg/m^3, gas dynamic viscosity is set to 1.7894×10^{-5} kg/m·s, and effect of gravity is not considered. The model inlet was set as the velocity inlet, wind speed was 4 m/s, outlet was set as the pressure outlet, initial surface pressure was set to 0, and other surfaces were set to no-slip fixed-wall boundary conditions. The dimensions of the physical model are shown in Fig. 4.

A turbulent pulsation signal uses the wind speed data of straight tunnels without external disturbances conducted by the author's team in the early stage. The experimental data were tested using a LDA. The laser beam generated by the sub-ion laser was divided into three pairs of six beams of monochromatic light, i.e., blue (LDA2), green (LDA1), and purple (LDA3), by a beam splitter, and the velocity components in the three directions of X (stream direction), Y (vertical direction), and Z (lateral direction) were measured. The light beam is sent into the transmitting probe through the transmission optical fiber and gathered at one point to form a measuring body. The scattered light signal generated by the tracer particles scattered in the flow field beforehand following the airflow through the measuring body is converted into an electrical signal by the photoelectric converter in the photoelectric receiver and transmitted to the signal processor and main control computer for analysis and processing to finally obtain the three-dimensional velocity component of the point with a velocity measurement accuracy of 0.1%. This is a laser measurement, and therefore, the flow field is not affected by external interference, speed measurement range is wide, and Doppler frequency is linearly related to the speed and unrelated to the temperature and pressure at that point. Therefore, LDA is currently the instrument with the highest speed measurement accuracy in the world and can better describe turbulent pulsating wind-speed data. The simulated wind speed and wind speed signals with added pulsating noise are shown in Fig. 5.

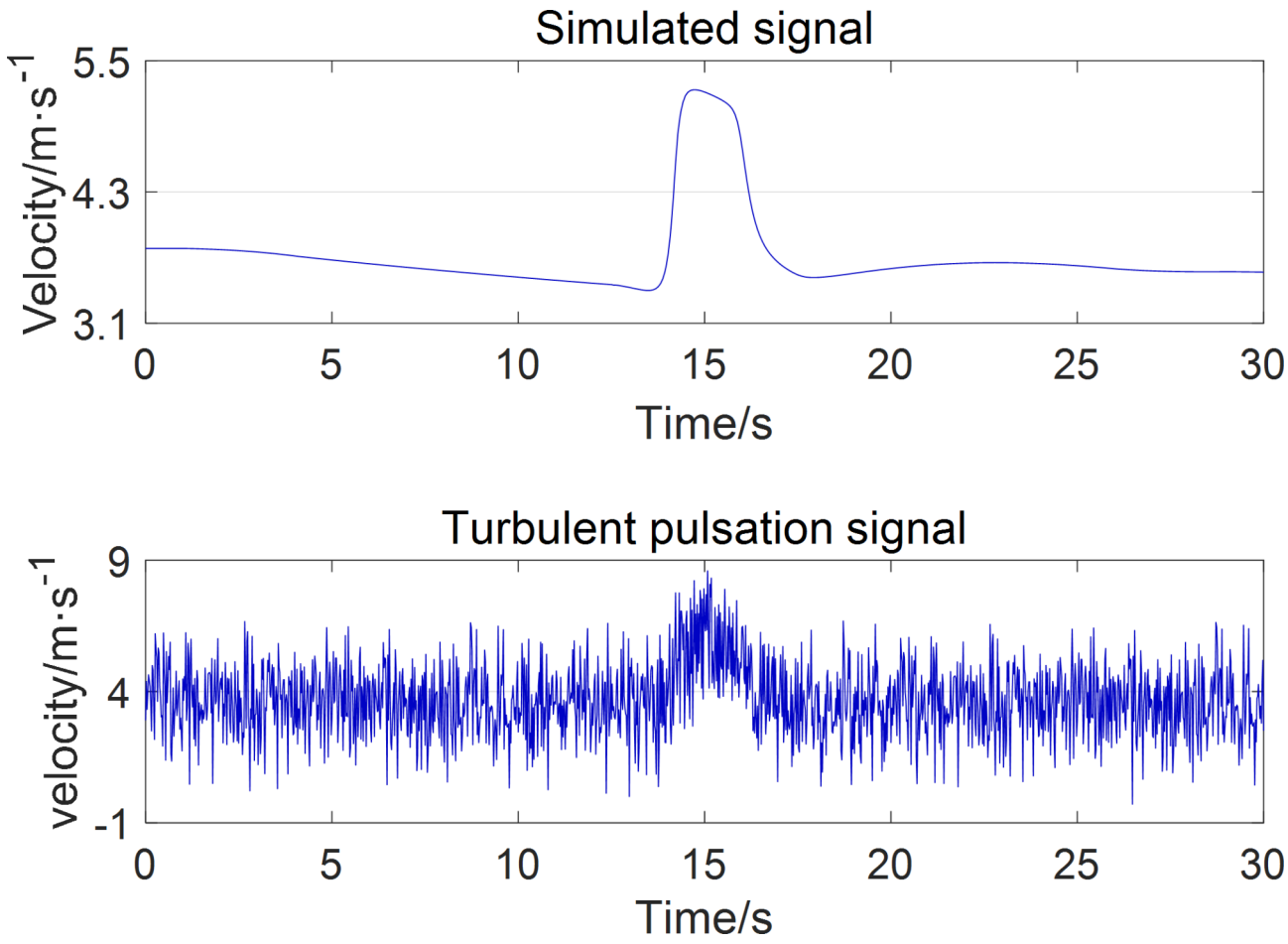


Fig. 5. Waveform diagram of a noisy signal.

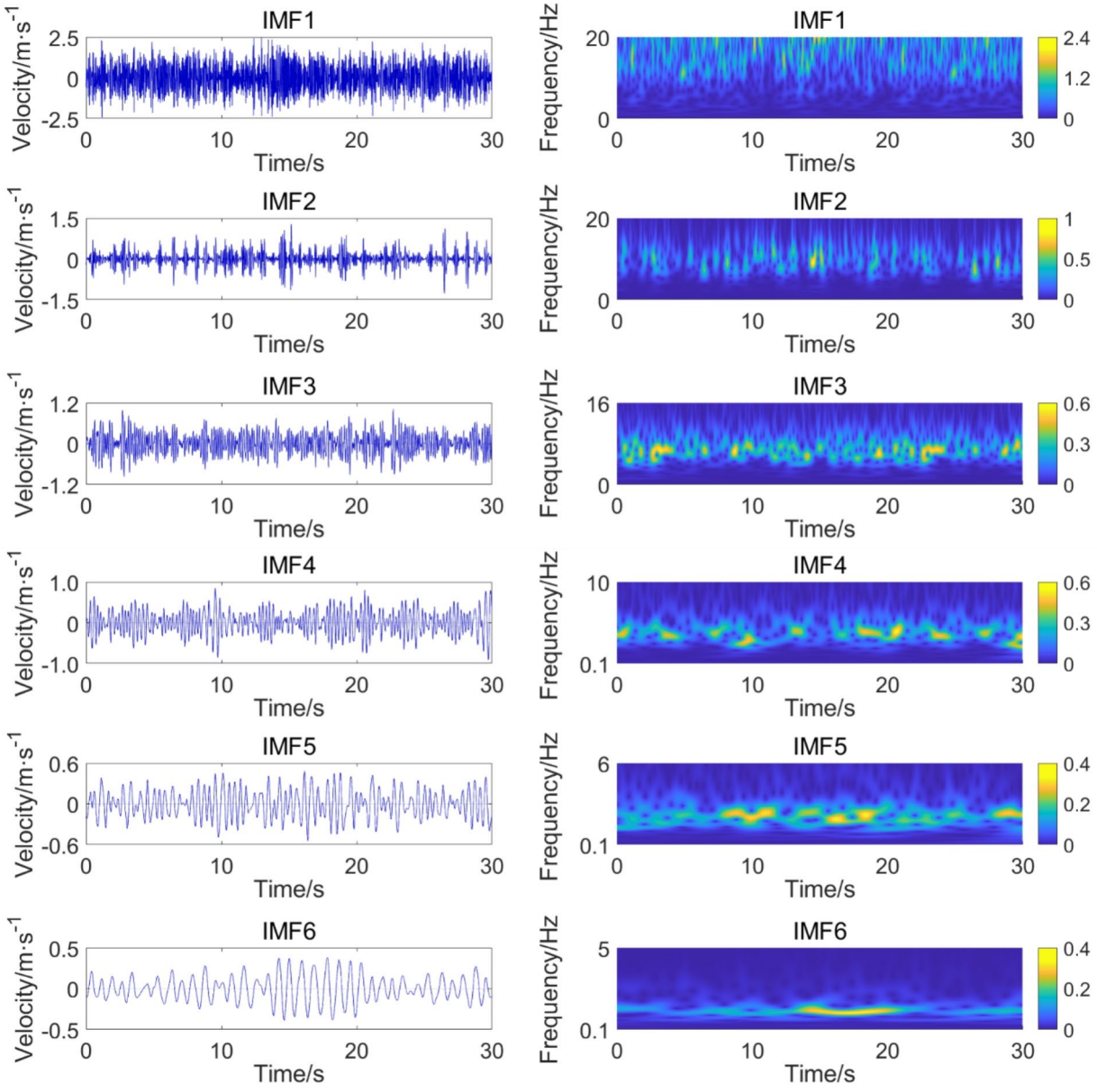


Fig. 6. CEEMDAN decomposes all IMF component waveforms and time-frequency graphs.

Evaluation indicators

Comparison indicators used in the joint denoising results and comparative analysis include the SNR and RMSE of the signals before and after denoising. SNR and RMSE are defined as

$$SNR = 10\log_{10}\left\{\frac{\sum_{n=1}^{N} s^2(n)}{\sum_{n=1}^{N}[s(n)-d(n)]^2}\right\}, \tag{17}$$

$$RMSE = \sqrt{\frac{\sum_{n=1}^{N}[s(n)-d(n)]^2}{N}}, \tag{18}$$

where $s(n)$ and $d(n)$ represent the amplitude of the nth sampling point of the noisy signal and amplitude of the nth sampling point of the signal after noise reduction, respectively.

SNR is a quantitative feature that describes signal denoising. The higher the SNR, the more information there is in the real signal, and the better is the denoising effect. The RMSE is the square root of the ratio of the square of the difference between the denoised and real signals to the number of acquisitions n. The smaller the RMSE, the closer is the denoising result to the real signal, and the better is the denoising effect.

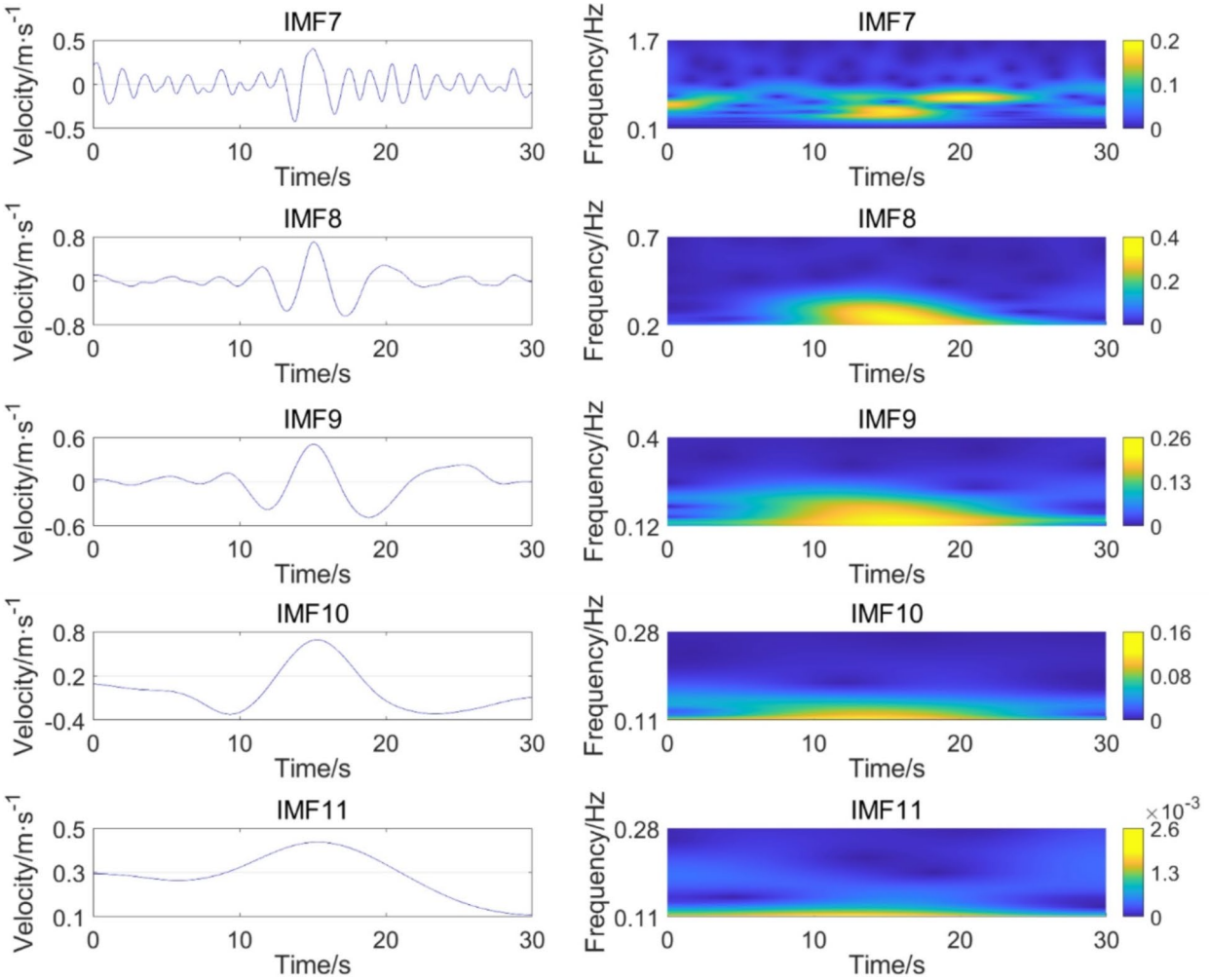


Figure 6. (continued)

IMF component	CMSE	IMF component	CMSE
IMF1	0.0830	IMF7	0.0506
IMF2	0.0988	IMF8	0.0464
IMF3	0.0825	IMF9	0.0828
IMF4	0.0419	IMF10	0.0928
IMF5	0.0247	IMF11	11.6572
IMF6	0.0197		

Table 1. Continuous mean square error for all IMF components.

Results and analysis

Joint denoising results and analysis

CEEMDAN decompose

The CEEMDAN algorithm is used for decomposing the simulation signal to obtain a series of IMF components. The CMSE value of each IMF component was calculated using Eq. (8), and the high-frequency IMF component to be denoised was determined based on the size of the CMSE value. The waveform and time-frequency diagram of 11 IMF components after CEEMDAN decomposition are presented in Fig. 6, and the CMSEs of the 11 IMF components are listed in Table 1.

Table 1 shows that the CMSE of the IMF6 component is the smallest. The CMSE criterion shows that the first 6 IMF components are components with more noise. Therefore, in the CEEMDAN-wavelet threshold joint denoising process, only the first six IMF components are subjected to wavelet threshold denoising. The waveforms and time frequencies of the first six IMF components after denoising are presented in Fig. 7. The

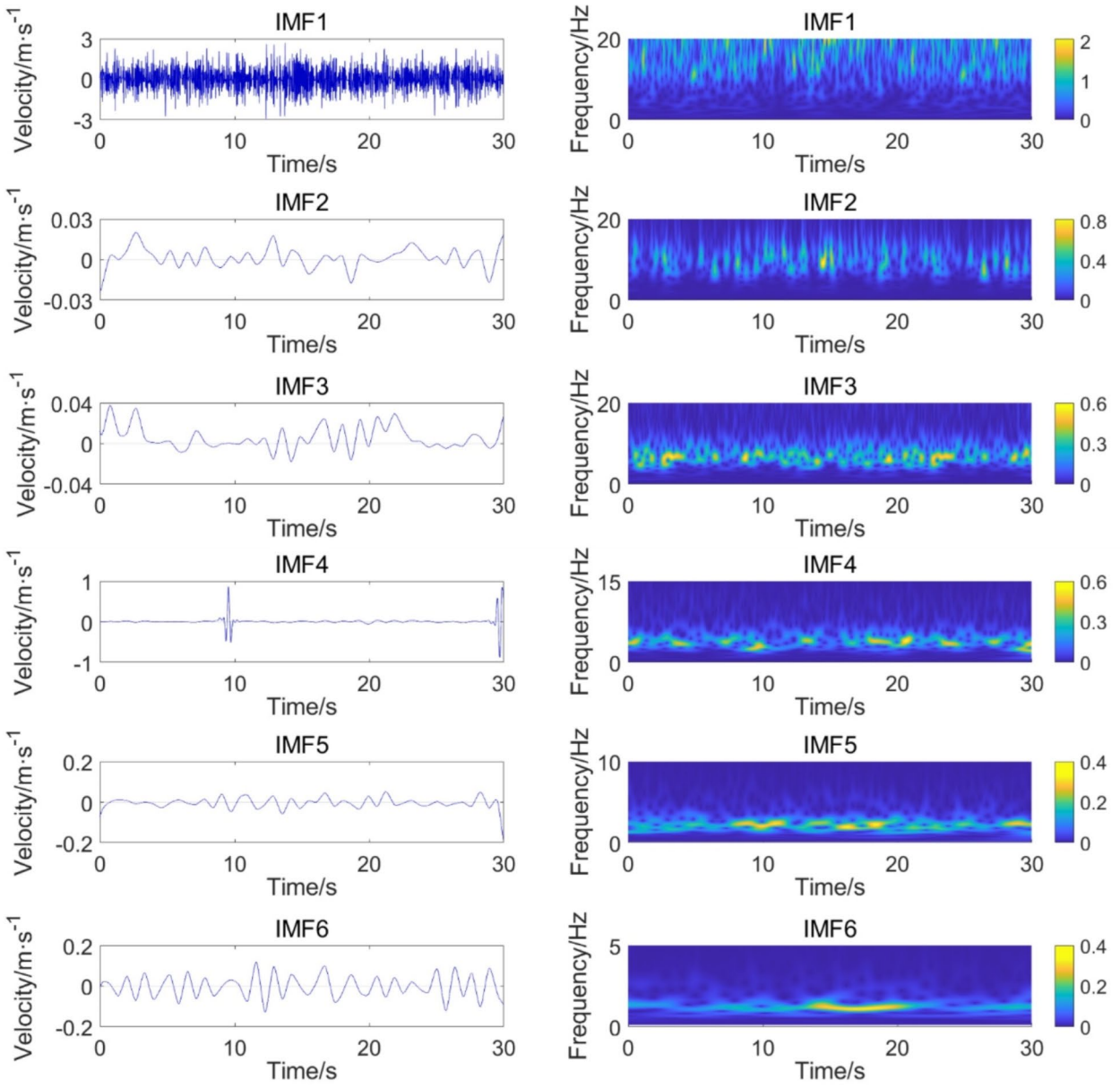


Fig. 7. Waveform and frequency graphs of the first 6 IMF components after noise reduction.

Daubechies (db)			Symlets (sym)			Coiflets (coif)			Biorthogonal (bior)		
Wavelet basis functions	SNR (dB)	RMSE	Wavelet basis functions	SNR (dB)	RMSE	Wavelet basis functions	SNR (dB)	RMSE	Wavelet basis functions	SNR (dB)	RMSE
db1	10.32	1.21	sym1	10.32	1.21	coif1	11.49	1.06	bior1.5	10.20	1.23
db2	10.45	1.19	sym2	10.45	1.19	coif2	11.57	1.05	bior2.8	10.48	1.19
db3	10.38	1.20	sym3	10.38	1.20	coif3	11.57	1.05	bior3.3	10.52	1.18
db4	12.35	0.96	sym4	11.52	1.05	coif4	11.58	1.05	bior3.5	10.65	1.16
db5	**12.60**	**0.93**	sym5	10.29	1.21	**coif5**	**11.64**	**1.04**	bior3.7	10.65	1.16
db6	11.16	1.10	**sym6**	**11.75**	**1.03**				bior3.9	10.79	1.14
db7	11.40	1.07	sym7	10.21	1.22				**bior5.5**	**12.84**	**0.90**
db8	11.54	1.05	sym8	11.74	1.03				bior6.8	11.66	1.04
db9	11.27	1.08	sym9	10.29	1.21						
db10	11.32	1.08	sym10	11.67	1.03						

Table 2. Comparison of the denoising effect of different wavelet basis functions. Significant values are in bold.

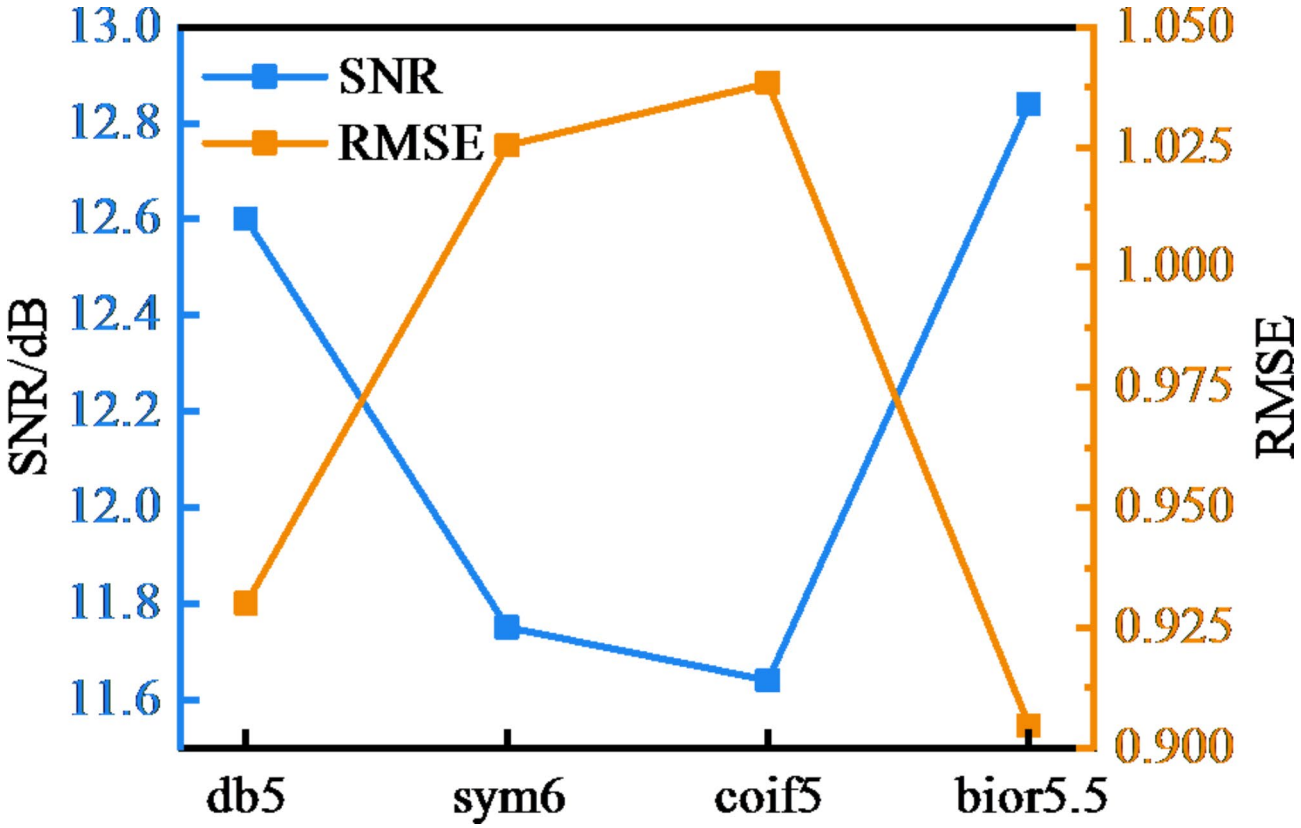


Fig. 8. Comparison of four wavelet basis function evaluation indices.

Decomposition level	SNR (dB)	RMSE
1	20.69	0.37
2	13.90	0.80
3	12.84	0.90
4	12.39	0.95
5	12.17	0.98
6	12.14	0.98
7	12.14	0.98
8	12.13	0.98
9	12.12	0.98
10	12.11	0.98

Table 3. Comparison of the denoising effect of different decomposition layers.

denoised IMF1, IMF2, IMF3, IMF4, IMF5, and IMF6 are reconstructed using the remaining IMF components to obtain the denoised pulsating signal.

Wavelet parameter selection

Wavelet basis function

The SNR, RMSE, and waveform similarity coefficient (NCC) are used as evaluation indicators to analyze the effect of different wavelet basis functions on the denoising effect of the wind speed sensor pulsation noise signal, and the control variable method is adopted for analyzing the denoising of the wind speed sensor simulation noise signal for four series of wavelet basis functions, i.e., Daubechies (db), Symlets (sym), Coiflets (coif), and Biorthogonal (bior), number of decomposition layers, threshold criteria, and threshold functions. In the denoising process, the number of wavelet decomposition layers was first set to three. The threshold was the rigidity threshold, and the threshold processing function was the soft threshold. The denoising effects of each wavelet function are listed in Table 2.

Table 2 shows that, among the db series wavelet basis functions, the db5 wavelet has the best denoising effect, with an SNR of 12.60 dB and an RMSE of 0.9300. Among the sym series wavelet functions, the sym6 wavelet has

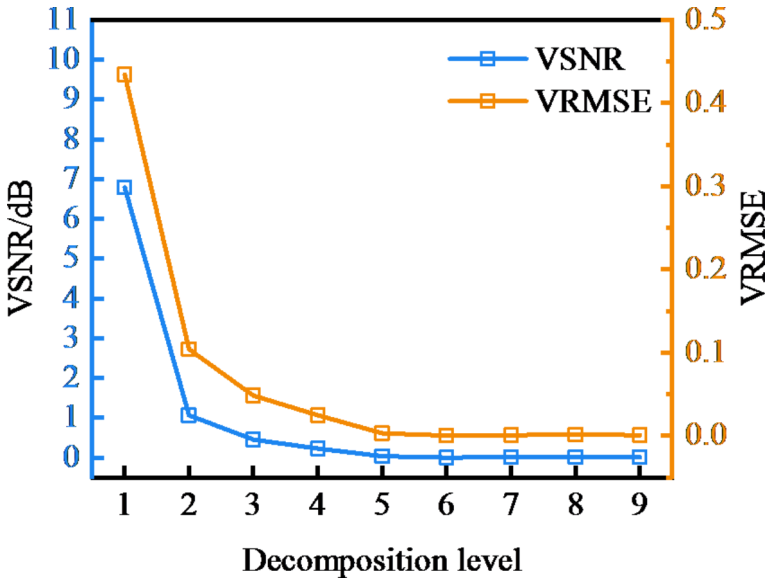


Fig. 9. Changes in each evaluation index with the number of decomposition layers under the bior5.5 wavelet basis function.

Threshold criteria	Threshold function	db5		sym6		coif5		bior5.5	
		SNR (dB)	RMSE	SNR (dB)	RMSE	SNR (dB)	RMSE	SNR (dB)	RMSE
Heursure	Soft threshold	9.81	1.28	9.82	1.28	9.82	1.28	9.81	1.28
	Hard threshold	9.81	1.28	9.90	1.27	9.90	1.27	9.81	1.28
Rigrsure	Soft threshold	11.94	1.00	11.21	1.09	11.11	1.10	12.17	0.98
	Hard threshold	12.84	0.91	12.73	0.92	12.29	0.96	12.87	0.90
Sqtwolog	Soft threshold	9.81	1.28	9.81	1.28	9.81	1.28	9.81	1.28
	Hard threshold	9.81	1.28	9.88	1.27	9.84	1.28	9.81	1.28
Minimaxi	Soft threshold	9.95	1.26	10.01	1.25	9.99	1.26	10.03	1.25
	Hard threshold	10.43	1.19	10.65	1.16	10.58	1.17	10.63	1.17

Table 4. Comparison of the denoising effect of the different threshold criteria and different threshold functions.

the best denoising effect, with an SNR of 11.75 dB and RMSE of 1.0254. Among the coif series wavelet functions, the coif5 wavelet has the best denoising effect, with an SNR of 11.64 dB and a RMSE of 1.0384. Among the bior series wavelet functions, the bior5.5 wavelet has the best denoising effect, with an SNR of 12.84 dB and RMSE of 0.9046. A horizontal comparison is shown in Fig. 8.

The bior5.5 wavelet function was used to analyze the decomposition layers of the pulsating noise signal.

Number of decomposition levels

In the denoising process, there will still be many noise signals in the signal if the number of decomposition layers is too small, whereas some effective information in the signal will be removed as noise if the number of decomposition layers is too large. The bior5.5 wavelet basis function is used to perform 1–10 layers of wavelet decompositions on the pulsating noise signal of the mine wind speed sensor to determine the optimal number of decomposition layers for denoising the pulsating noise signal of the mine wind speed sensor. The denoising effects for different numbers of layers are listed in Table 3.

Table 3 indicates that the overall trend of the denoising evaluation index of the pulsating noise signal of the mine wind speed sensor was the same as that of the number of decomposition layers. However, the rate of change with the number of decomposition layers was different. This study used the change in the SNR (VSNR) and change in the RMSE (VRMSE) as the denoising effect evaluation indicators. In the actual denoising process, the VSNR and VRMSE showed obvious convergence with an increase in the number of decomposition layers; i.e., the changes in VSNR and VRMSE were not obvious after the signal was over-denoised.

VSNR(m) and VRMSE(m) are expressed as

$$VSNR(m) = |SNR(m+1) - SNR(m)|, \tag{19}$$

$$VRMSE(m) = |RMSE(m+1) - RMSE(m)|, \tag{20}$$

where VSNR (m) represents the change in the SNR between scale m + 1 and scale m and VRMSE (m) represents the change in the RMSE between scale m + 1 and scale m. The VSNR and VRMSE under the bior5.5 wavelet basis function in Table 3 were calculated to analyze the effect of the number of decomposition layers on the denoising effect of the pulsating noise signal of the mine wind speed sensor. The changing trends of the VSNR and VRMSE with the number of decomposition layers are presented in Fig. 9.

Figure 9 shows that the overall trends of the VSNR and VRMSE changes with the decomposition layer are consistent under different wavelet basis functions, and both tend to be stable after the 5th value. Therefore, the optimal number of decomposition layers for the pulsating noise signal of the mine wind speed sensor can be considered to be five or six. Five decomposition layers were selected in this study to reduce the number of calculations in the denoising process of the pulsating noise signal of the mine wind speed sensor.

Threshold and threshold functions

Four commonly used threshold criteria were used to perform soft and hard threshold denoising analysis on the pulsation noise signal of the mine wind speed sensor based on the bior5.5 wavelet, wavelet basis function, and five decomposition levels. The SNR and RMSE values of the denoised signals are listed in Table 4.

Comparing the denoising results presented in Table 4 reveals that (a) the overall denoising effect of the hard threshold function is better than that of the soft threshold function when the threshold criteria are identical; (b) the overall denoising effect under the risk criterion was the best when the threshold functions were the same; (c) the threshold criterion is rigorous, the threshold function is a hard threshold, and pulsation noise signal denoising effect is optimal when the wavelet function is bior5.5. Therefore, the hard threshold under the wavelet function bior5.5 and the rigor threshold rule are the most suitable for the denoising analysis of the pulsation noise signal of the mine wind speed sensor.

Joint denoising results and analysis

Based on the above analysis, the optimal parameters for denoising the pulsating noise signal of the mine wind-speed sensor using the CEEMDAN-wavelet threshold are as follows: the wavelet basis function is bior5.5, number of decomposition levels is five, and risk criterion and hard threshold are used. Meanwhile, the SNR was 12.87 dB, and the RMSE was 0.90. The waveform and time-frequency diagrams before and after denoising are presented in Fig. 10.

Comparing the waveforms revealed that the noise amplitude in the signal processed by the CEEMDAN-wavelet threshold joint denoising method is significantly reduced. This shows that the turbulent pulsation noise in the wind speed signal can be suppressed effectively by using the method, and the disturbance waveform caused by the passing of the mine car can be maintained. From the analysis of evaluation indicators, the SNR improved by 13.40 dB after denoising, and the RMSE reduced from the original 1.31 to 0.90. However, the higher the signal-to-noise ratio, the greater the ratio of the useful signal detected by the sensor to the pulsating noise, the lower the root-mean-square error is, the smaller the deviation between the wind speed measured by the sensor and the actual value. Therefore, the combined noise reduction method of CEEMDAN-wavelet threshold has a certain noise reduction effect on the mine airflow turbulence ripple noise signal, which means that the mine wind speed sensor, as an intelligent sensing equipment, can provide more accurate and effective wind speed data for the mine intelligent ventilation system, and provide reliable basic data support for the mine intelligent ventilation system.

Feasibility verification and comparative analysis

Because the instantaneous value of turbulent pulsation signal is normally distributed and the power spectral density is uniformly distributed, the turbulent pulsation signal is similar to Gaussian white noise. Therefore, in order to further prove the effectiveness of the noise reduction method presented in this paper, Gaussian white noise with SNR of 4, 6 and 8 dB is added to the simulation signal shown in Fig. 5 to represent turbulence pulsation noise with different turbulence pulsation intensification. Three groups of simulation experiments

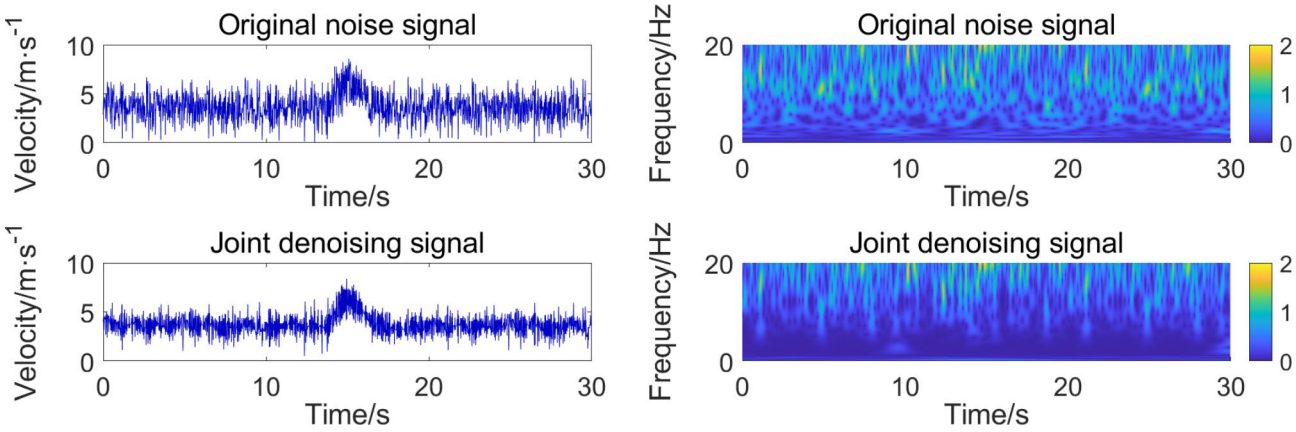


Fig. 10. Waveform diagram and time-frequency diagram before and after noise reduction.

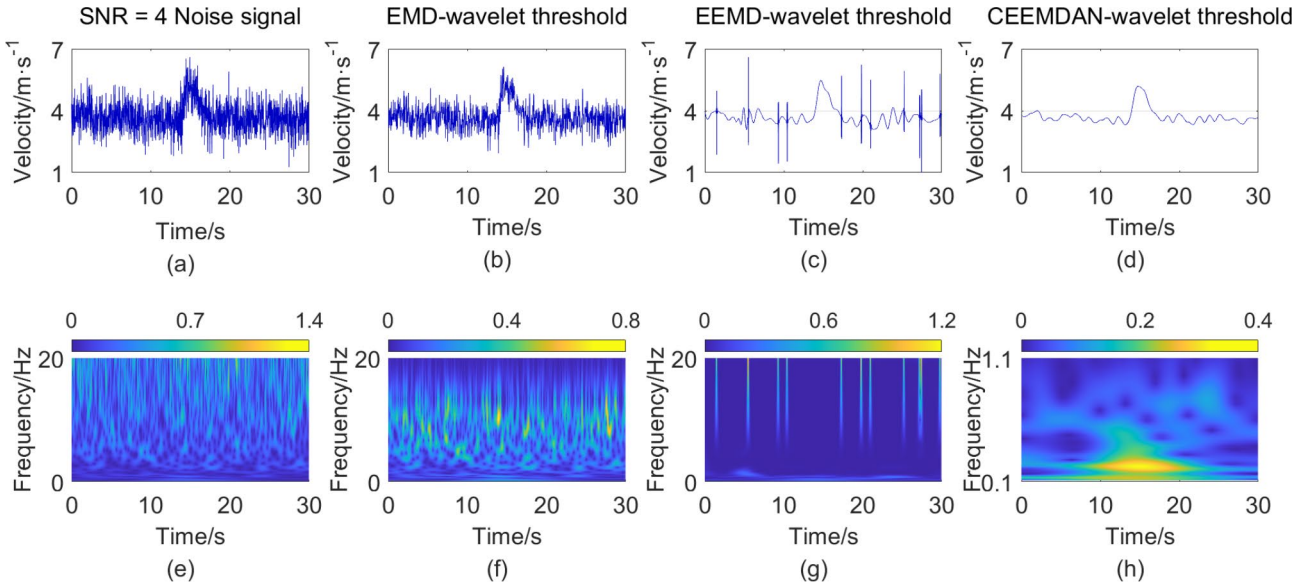


Fig. 11. Comparison of SNRs for 4 dB noise reduction effects.

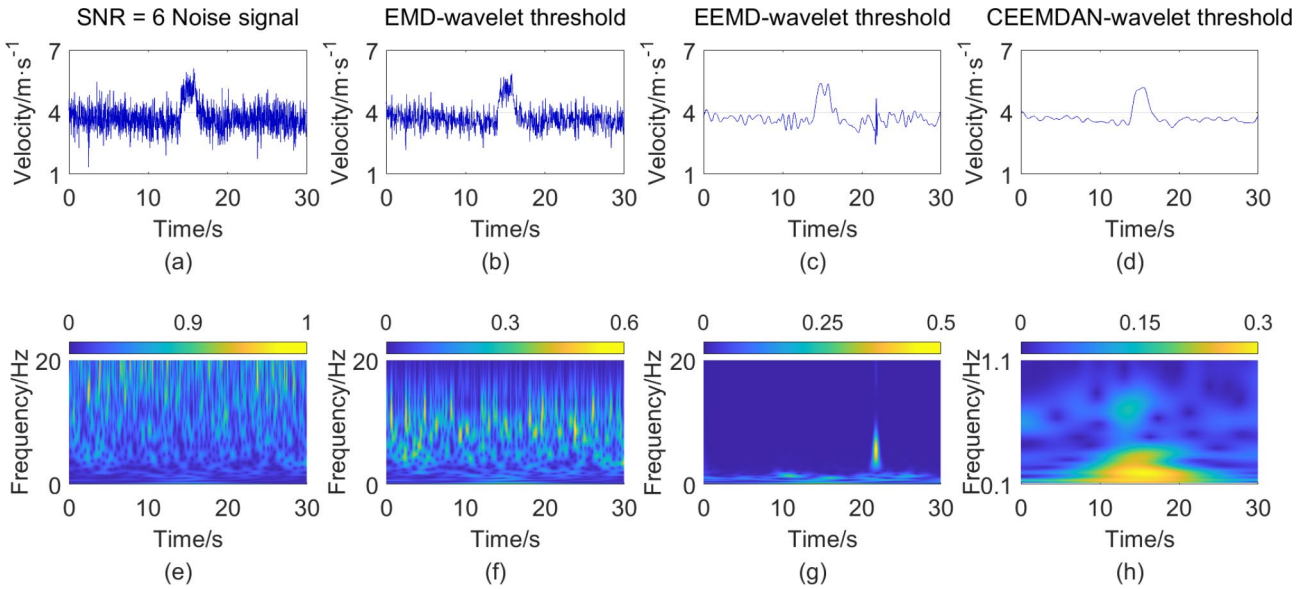


Fig. 12. Comparison of SNRs for 6 dB noise reduction effects.

were conducted for comparing and analyzing the denoising effects of the EMD-, EEMD-, and CEEMDAN-wavelet threshold methods. The results of the three groups of experiments are shown in Figs. 11, 12 and 13, respectively. Figure 11a–d show the signal waveform when the SNR is 4 dB after adding noise, after denoising by the EMD-wavelet threshold method, after denoising by the EEMD-wavelet threshold method, after denoising by the CEEMDAN-wavelet threshold method, respectively. Figure 11e–h show the time-frequency diagrams corresponding to the above waveforms.

After the experiment, the SNR and RMSE of each group of signals were obtained, and the evaluation parameters of each group of signals after denoising were plotted as a bar graph, as shown in Fig. 14. Figure 14a and b show a comparison of the SNR and RMSE data after adding 4, 6, and 8 dB noise, respectively.

Analyzing the experimental data in Fig. 14 shows that the three methods can increase the SNR to more than 20 dB after noise reduction when the SNR is 8 dB before noise reduction, and the RMSE of the signal after noise reduction is below 0.3, indicating that the three methods have good noise reduction effects. However, with a decrease in SNR, there are more random noise components in the signal when the SNR of the signal before denoising is 4 dB. After denoising using the EMD- and EEMD-wavelet threshold methods, the RMSEs reached 0.46 and 0.38 although the SNRs after denoising reached 18.27 and 19.96 dB, respectively.

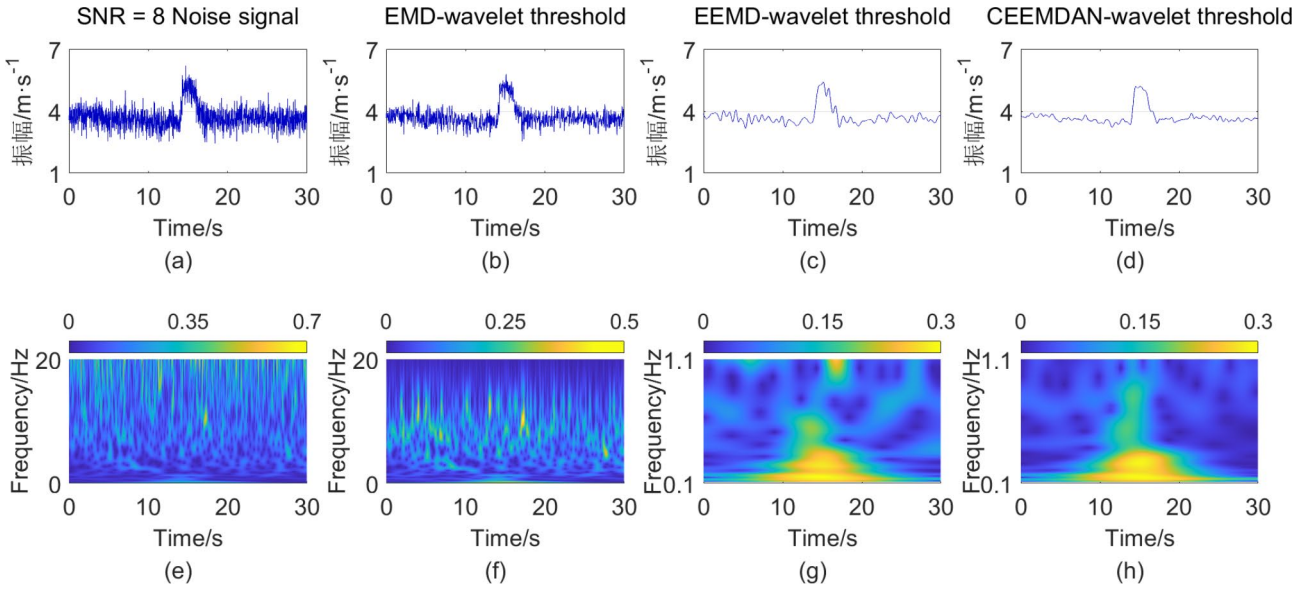


Fig. 13. Comparison of SNR for 8 dB noise reduction effects.

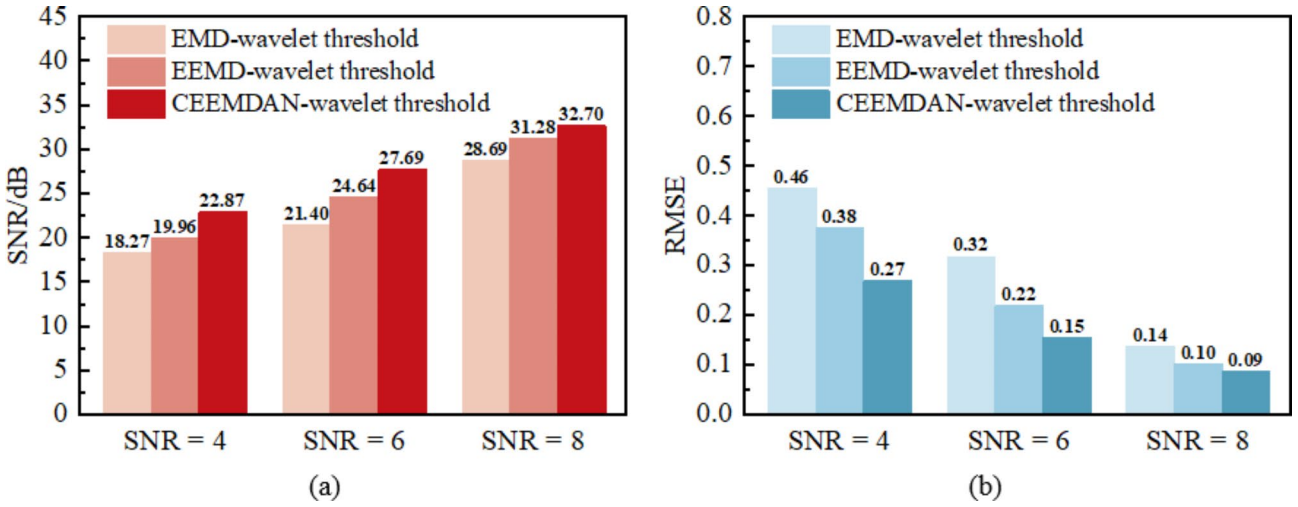


Fig. 14. Comparison of the noise reduction results of different noise reduction methods.

Ness of the mine car disturbance waveform, increasing the difficulty of identifying disturbances in the mine wind speed sensor signal. Although the proposed method effectively suppresses these defects, it better maintains the waveform of the original signal, with obvious peak features and better smoothness, indicating that the method in this paper has a better noise reduction effect.

Noise reduction and analysis of on-site wind speed sensor data

EMD- wavelet, EEMD- wavelet, and CEEMDAN-wavelet denoising were used to denoise the ultrasonic wind speed sensor monitoring data in the auxiliary transport lane of a mine for verifying the denoising effect and feasibility of the proposed method for actual underground wind speed sensor monitoring data. The onsite wind speed sensor is illustrated in Fig. 15. The sensor was arranged on the top plate of the auxiliary transport lane, and the test point was placed at the cross-sectional average wind speed ring. The multiparameter differential pressure sensor is shown on the left. The wind speed data after denoising using the three methods are plotted in the same coordinate system for comparative analysis, as shown in Fig. 16.

As can be seen from the waveform diagram of wind speed data in Fig. 16, since decomposition conditions are not satisfied in the process of obtaining upper and lower envelope lines in EMD decomposition, mode aliasing effect occurs in the decomposition process, resulting in different frequency components coexisting in the same IMF component, and a large amount of high-frequency information is lost. Therefore, its waveform can only roughly depict the overall wind speed variation trend. After EEMD-wavelet threshold denoising, the noise is not removed at some places where the wind speed has slight pulsation changes; however, the peak value of the wind

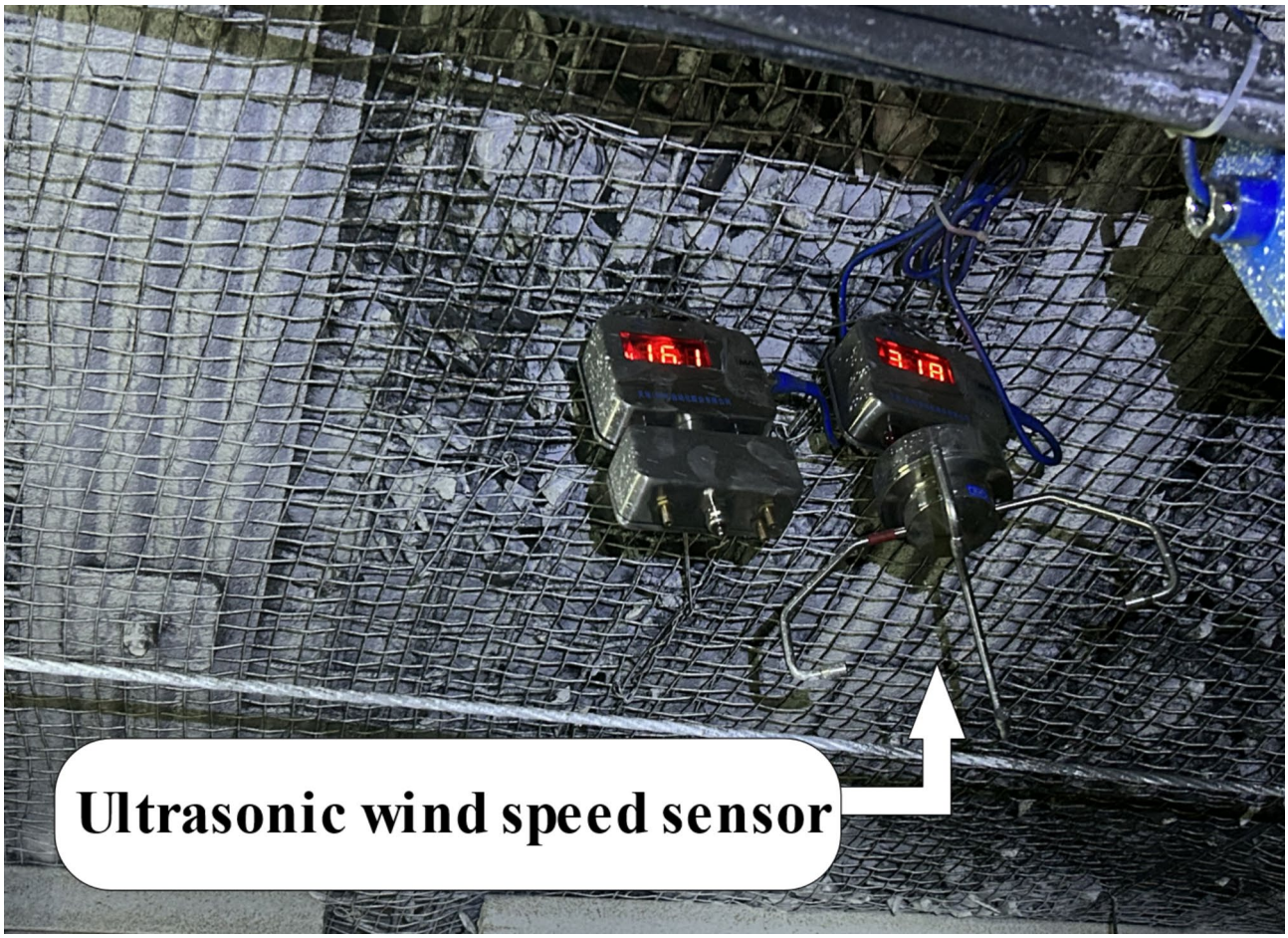


Fig. 15. Ultrasonic wind speed sensor in auxiliary transportation lane of a mine.

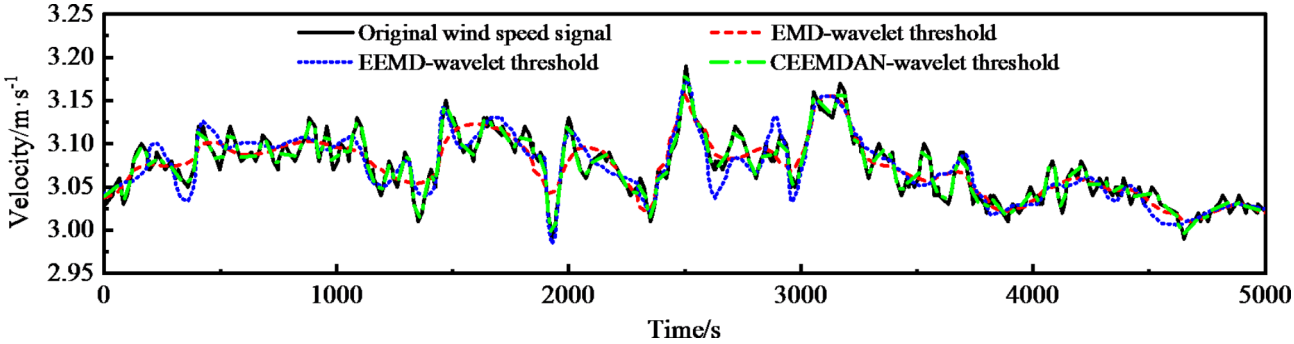


Fig. 16. Noise reduction comparison of the field wind speed sensor data.

speed at this place is significantly increased or decreased, thereby resulting in abnormal wind speed data during this period. When the wind speed data fluctuates with a small amplitude, its waveform produces hysteresis. CEEMDAN-wavelet threshold denoising can clearly depict the disturbance waveform and filter out the pulsating noise data at the pulsating location. Therefore, the denoising method proposed in this study has a certain effect on the noise filtering of underground wind-speed sensor monitoring data and provides a feasible method for data denoising for intelligent sensing equipment in mine intelligent ventilation systems.

Discussion

The proposed method achieved the best noise reduction effect and achieved a good noise reduction effect when applied to the ultrasonic wind speed sensor monitoring data of the actual auxiliary transportation tunnel of the mine regardless of whether it is the result analysis of denoising from the simulation signal plus

experimental pulsating noise, or the result analysis of denoising from the simulation signal plus simulated noise. However, data signals obtained from the simulation and experiment were significantly different from the actual monitoring data signals of on-site sensors. The temperature, humidity, atmospheric pressure, and other meteorological conditions in the underground tunnels, as well as the complex coupling environment, such as production activities, significantly affect actual on-site monitoring data. On-site wind speed sensors cannot reach the test accuracy and sensitivity of the laboratory LDA and monitor and identify a large number of pulsating noise signals. Further, it is unknown if the wind speed sensor manufacturer sets up a data-processing function before the wind speed sensor leaves the factory. Finally, according to Article 495 of the Coal Mine Safety Regulations[41], the safety monitoring system must upload monitoring data in real time. Therefore, the wind-speed sensor manufacturer sets up data-uploading principles. In the monitoring process, when the wind speed changes, the changed wind speed will be uploaded to the monitoring system. Combine the above three points, the method presented in this paper has certain limitations in denoising the monitoring data of on-site wind speed sensors. There are significant differences between the experimental and simulated wind speed pulsation noise signals and on-site sensor monitoring data. However, as can be seen from Fig. 16, for field data, the noise reduction method proposed in this paper basically retains the original waveform characteristics on the basis of filtering out relatively small fluctuating wind speeds, which also provides a data optimization method for the identification of mine airflow disturbance. Therefore, noise reduction methods and parameter selection under different conditions, such as the continuous improvement and updating of mine wind speed sensors, and the purpose of the tunnels where the wind speed sensors are located, are subjects of further in-depth research.

The existing filtering methods of mine wind speed sensor include Kalman filter, wavelet threshold and other methods, and relevant researches have achieved remarkable results. However, these researches have not analyzed and studied the roadway air flow and wind speed sensor from the nature of turbulent pulsation. Meanwhile, the traditional denoising methods are not effective in dealing with non-stationary and nonlinear signals. In the process of noise reduction, a large number of disturbed signals are regarded as noise and filtered together. By combining the advantages of CEEMDAN decomposition and wavelet threshold denoising, the joint denoising method proposed in this paper can better capture the local features of non-stationary and nonlinear signals, and can adaptively select the threshold value according to the characteristics of the signal, so as to better retain the details of the signal and effectively remove the noise, thus improving the accuracy and flexibility of denoising. In the field of mine, the CEEMDAN-wavelet threshold denoising method can also be used to reduce the noise processing of toxic and harmful gas sensor monitoring data, mine microseismic signals, main fan vibration and noise signals. Besides mine field, the method can also be applied to underwater Lidar echo signal, ball mill cylinder vibration signal, in situ ultrasonic detection signal of hydraulic generator set and so on. In addition, in some other scenarios that are sensitive to signal noise, such as fault diagnosis, speech recognition, biomedical signal processing, financial data analysis, etc., CEEMDAN-wavelet threshold denoising method may also have potential application value. However, in practical application, appropriate adjustment and optimization should be carried out according to the characteristics and requirements of specific problems.

Conclusion

(1) Wavelet parameters are optimized using the control variable method when the CEEMDAN-wavelet threshold joint denoising method is used for reducing the pulsation noise of the mine wind speed sensor. When the wavelet basis function is bior5.5, the number of decomposition levels is five, threshold criterion is the rigor criterion, and threshold function is the hard threshold, and it is most suitable for denoising the pulsation noise signal of the mine wind speed sensor.

(2) Different joint denoising methods were used for denoising the noise signals with SNR = 4, 6, and 8. When 4 dB of noise was added, the SNRs of the EMD-, EEMD- and CEEMDAN-wavelet thresholding methods after denoising were 18.27, 21.40, and 28.69 dB, respectively, and the corresponding RMSEs were 0.46, 0.32, and 0.14, respectively. When 6 dB of noise was added, the SNRs were 19.96, 24.64, and 31.28 dB, and the corresponding RMSEs were 0.38, 0.22, and 0.10, respectively. When 8 dB of noise was added, the SNRs were 22.87, 27.69, and 32.70 dB, and the corresponding RMSEs were 0.27, 0.15, and 0.09, respectively. The joint denoising method can effectively eliminate the modal aliasing phenomenon and maintain the smoothness of the disturbed waveform. Further, this method can maintain the waveform of the original signal better, with obvious peak characteristics and good smoothness, and it has a good denoising effect.

(3) The use of the CEEMDAN-wavelet threshold joint denoising had a positive effect on denoising the on-site mine wind speed sensor data. This study proposes a new method for data denoising and preprocessing of mine wind speed sensors and enriches the data processing function of intelligent sensing equipment in mine intelligent ventilation systems.

Data availability

All relevant data are within the paper.

Received: 18 June 2024; Accepted: 3 October 2024
Published online: 22 October 2024

References

1. Wang, G. New technological progress of coal mine intelligence and its problems. *Coal Sci. Technol.* **50**, 1–27 (2022).
2. Zhou, F. et al. Principle, key technology and preliminary realization of mine intelligent ventilation. *J. China Coal Soc.* **45**, 2225–2235 (2020).
3. Liu, J. Overview on key scientific and technical issues of mine intelligent ventilation. *Saf. Coal Mines* **51**, 108–111 (2020).

4. Liu, J. et al. Resistance variant fault diagnosis of mine ventilation system and position optimization of wind speed sensor. *J. China Coal Soc.* **46**, 1907–1914 (2021).
5. Li, L., Jian, L., Qichao, Z. & De, H. Influence of sample attributes on generalization performance of machine learning models for windage alteration fault diagnosis of the mine ventilation system. *Expert Syst. Appl.* **213**, (2023).
6. Huang, D., Liu, J., Deng, L., Li, X. & Song, Y. Application of adaptive Kalman filter in online monitoring of mine wind speed. Preprint at https://doi.org/10.20944/preprints201903.0048.v1 (2019).
7. Li, J. et al. Accurate and real-time network calculation for mine ventilation without wind resistance measurement. *J. Wind Eng. Ind. Aerodyn.* **230**, 105183 (2022).
8. SDAE Cleaning model. Of wind speed monitoring data in the mine monitoring system. *Arch. Min. Sci.* https://doi.org/10.24425/ams.2023.146178 (2023).
9. Deng, L., Yuan, J., Liu, J. & Shang, W. Detection method of wind speed anomaly fluctuation based on SSA-LSTM. *Coal Sci. Technol.* 1–9.
10. Wei, Z., Yucheng, L. & Junqiao, L. Data processing method of mine wind speed monitoring based on an improved fuzzy C-means clustering algorithm. *Appl. Sci.* **12**, (2022).
11. Zhang, W. et al. Comparison of structured data noise reduction methods for airflow speed sensor of intelligent ventilation. *J. Saf. Sci. Technol.* **17**, 70–76 (2021).
12. Liu, J., Li, X., Song, Y., Gao, K. & Deng, L. Experimental study on uncertainty mechanism of mine airvelocity and pressure with non-external disturbance. *J. China Coal Soc.* **41**, 1447–1453 (2016).
13. Cao, P. & Liu, J. Research on minimum balance correction of air volume of mine sensor. *J. Saf. Environ.* 1–15. https://doi.org/10.13637/j.issn.1009-6094.2023.2008
14. Ying, M., Feng, G., Jian, S., Huo, X. & Ma, C. Real-time research of diesel engine vibration signal denoising by wavelet based on DSP. *Trans. CSICE* **40**, 345–350 (2022).
15. Liu, J., Yao, Y., Li, P. & Liu, J. Parameter optimization wavelet denoising algorithm for full-waveforms data of laser altimetry satellite. *Chin. J. Lasers* **48**, 128–139 (2021).
16. Priyadarshini, M. S., Bajaj, M., Prokop, L. & Berhanu, M. Perception of power quality disturbances using Fourier, Short-Time Fourier, continuous and discrete wavelet transforms. *Sci. Rep.* **14**, 3443 (2024).
17. Dai, B., Frusque, G., Li, Q. & Fink, O. Acceleration-guided acoustic signal denoising framework based on learnable wavelet transform applied to slab track condition monitoring. *IEEE Sens. J.* **22**, 24140–24149 (2022).
18. Dodda, V. C., Kuruguntla, L., Mandpura, A. K. & Elumalai, K. Simultaneous seismic data denoising and reconstruction with attention-based wavelet-convolutional neural network. *IEEE Trans. Geosci. Remote Sens.* **61**, 1–14 (2023).
19. Qin, Z. et al. A method for analyzing pressure fluctuation signals based on wavelet transform. *J. Beijing Univ. Aeronaut. Astronaut.* 1–11 https://doi.org/10.13700/j.bh.1001-5965.2023.0781
20. Yu, B. & Yang, X. The Hilbert transform of B-spline wavelets. *IEEE Signal. Process. Lett.* **28**, 693–697 (2021).
21. Liu, J. W., Zuo, F. L., Guo, Y. X., Li, T. Y. & Chen, J. M. Research on improved wavelet convolutional wavelet neural networks. *Appl. Intell.* **51**, 4106–4126 (2021).
22. Zhou, H., Chabory, A. & Douvenot, R. A fast wavelet-to-wavelet propagation method for the simulation of long-range propagation in low Troposphere. *IEEE Trans. Antennas Propagat.* **70**, 2137–2148 (2022).
23. Vashishtha, G., Chauhan, S., Kumar, A. & Kumar, R. An ameliorated African vulture optimization algorithm to diagnose the rolling bearing defects. *Meas. Sci. Technol.* **33**, 075013 (2022).
24. Vashishtha, G. & Kumar, R. Autocorrelation energy and aquila optimizer for MED filtering of sound signal to detect bearing defect in Francis turbine. *Meas. Sci. Technol.* **33**, 015006 (2022).
25. Vashishtha, G. & Kumar, R. Pelton wheel bucket fault diagnosis using improved Shannon Entropy and expectation maximization principal component analysis. *J. Vib. Eng. Technol.* **10**, 335–349 (2022).
26. Huang, N. et al. (ed, E.) The empirical mode decomposition and the Hilbert spectrum for nonlinear and non-stationary time series analysis. *Proc. R Soc. Lond. A* **454** 903–995 (1998).
27. Yue, G. O. N. G. et al. To suppress the random noise in microseismic signal by using empirical mode decomposition and wavelet transform. *J. China Coal Soc.* **43**, 3247–3256 (2018).
28. Liu, X., Zhang, Y. & Zhang, Q. Comparison of EEMD-ARIMA, EEMD-BP and EEMD-SVM algorithms for predicting the hourly urban water consumption. *J. Hydroinformatics* **24**, 535–558 (2022).
29. Niu, D., Wang, K., Sun, L., Wu, J. & Xu, X. Short-term photovoltaic power generation forecasting based on random forest feature selection and CEEMD: A case study. *Appl. Soft Comput.* **93**, 106389 (2020).
30. Li, Y., Han, L. & Liu, X. Accuracy enhancement and feature extraction for GNSS daily time series using adaptive CEEMD-multi-PCA-based filter. *Remote Sens.* **15**, 1902 (2023).
31. Liu, H., Mi, X. & Li, Y. Comparison of two new intelligent wind speed forecasting approaches based on wavelet packet decomposition, complete ensemble empirical mode decomposition with adaptive noise and artificial neural networks. *Energy Convers. Manag.* **155**, 188–200 (2018).
32. Wenjun, B. & Yingjie, C. Denoising of blasting vibration signals based on CEEMDAN-ICA algorithm. *Sci. Rep.* **13**, 20928 (2023).
33. Wuge, C., Junning, L., Qian, W. & Ka, H. Fault feature extraction and diagnosis of rolling bearings based on wavelet thresholding denoising with CEEMDAN energy entropy and PSO-LSSVM. *Measurement* **172**, (2021).
34. Yang, Z., Lin, J., Wang, K., Cheng, Z. & Liu, P. De-noising of concrete acoustic emission signals based on CEEMD-wavelet packet adaptive threshold. *J. Vib. Shock* **42**, 139–149 (2023).
35. Vashishtha, G. & Kumar, R. Unsupervised learning model of sparse filtering enhanced using Wasserstein distance for intelligent fault diagnosis. *J. Vib. Eng. Technol.* **11**, 2985–3002 (2023).
36. Randall, R. B. & Antoni, J. Why EMD and similar decompositions are of little benefit for bearing diagnostics. *Mech. Syst. Signal. Process.* **192**, (2023).
37. Wu, Z. & Huang, N. E. Ensemble empirical mode decomposition: A noise-assisted data analysis method. *Adv. Adapt. Data Anal.* **01**, 1–41 (2009).
38. Yeh, J. R., Shieh, J. S. & Huang, N. E. Complementary ensemble empirical mode decomposition: A novel noise enhanced data analysis method. *Adv. Adapt. Data Anal.* **02**, 135–156 (2010).
39. Torres, M. E., Colominas, M. A., Schlotthauer, G. & Flandrin, P. A complete ensemble empirical mode decomposition with adaptive noise. In *IEEE International Conference on Acoustics, Speech and Signal Processing (ICASSP)* 4144–4147 (IEEE, Prague, Czech Republic, 2011). https://doi.org/10.1109/ICASSP.2011.5947265 (2011).
40. Boudraa, A. O. & Cexus, J. C. EMD-based signal filtering. *IEEE Trans. Instrum. Meas.* **56**, 2196–2202 (2007).
41. Coal Mine Safety Regulations. *China Legal Publishing House* (2022).

Acknowledgements

This paper is financially supported by the Natural Science Foundation of China (No. 51574142, No. 51774169, No. 52104194).

Author contributions

Y.W.: Methodology, Data Curation, Experimental, Writing original draft, Writing-review & editing. J.L.: Project administration, Funding acquisition. D.W.: Conceptualization, Supervision. X.L.: Numerical simulation. P.C.: Programme. K.H.: Data test.

Declarations

Competing interests

The authors declare no competing interests.

Additional information

Correspondence and requests for materials should be addressed to J.L.

Reprints and permissions information is available at www.nature.com/reprints.

Publisher's note Springer Nature remains neutral with regard to jurisdictional claims in published maps and institutional affiliations.

Open Access This article is licensed under a Creative Commons Attribution-NonCommercial-NoDerivatives 4.0 International License, which permits any non-commercial use, sharing, distribution and reproduction in any medium or format, as long as you give appropriate credit to the original author(s) and the source, provide a link to the Creative Commons licence, and indicate if you modified the licensed material. You do not have permission under this licence to share adapted material derived from this article or parts of it. The images or other third party material in this article are included in the article's Creative Commons licence, unless indicated otherwise in a credit line to the material. If material is not included in the article's Creative Commons licence and your intended use is not permitted by statutory regulation or exceeds the permitted use, you will need to obtain permission directly from the copyright holder. To view a copy of this licence, visit http://creativecommons.org/licenses/by-nc-nd/4.0/.

© The Author(s) 2024